https://doi.org/10.5194/egusphere-2024-2636
Preprint. Discussion started: 29 August 2024

The Critical Number and Size of Precipitation Embryos to Accelerate Warm Rain Initiation

Jung-Sub Lim[1, 2], Yign Noh[2], Hyunho Lee[3], and Fabian Hoffmann[1]
[1]Meteorologisches Institut, Ludwig-Maximilians-Universität, München, Germany.
[2]Department of Atmospheric Sciences, Yonsei University, Seoul, Republic of Korea.
[3]Department of Atmospheric Sciences, Kongju National University, Gongju-si, Chungcheongnam-do, Republic of Korea.
Correspondence: Yign Noh (noh@yonsei.ac.kr) and Fabian Hoffmann (Fa.hoffmann@lmu.de)

Abstract. Understanding warm rain initiation through droplet collision and coalescence is a fundamental yet complex challenge in cloud microphysics. Although it is well-known that sufficiently large droplets, so-called precipitation embryos (PEs), may accelerate droplet collisions, it is uncertain how many and how large these PEs should be to affect rain initiation substantially. We address this question using an ensemble of box simulations with Lagrangian cloud microphysics. We found that the warm rain initiation is substantially accelerated only if the PE size or number (or the product of those) exceeds a critical threshold necessary to compensate for the PE-induced suppression of collisions among non-PEs. The sensitivity of this threshold to the shape of the droplet size distribution and turbulence effects on the collision process is analyzed. It is shown that more and larger PEs are needed when collisions are already efficient without PEs. Beyond increasing our fundamental understanding of the precipitation process in warm clouds, our results may help to constrain the effect of PE-like particles intentionally or unintentionally added in geoengineering approaches, such as rain enhancement or marine cloud brightening.

1 Introduction

A key question in warm rain initiation is to explain the growth of cloud droplets in the radius range between 15 and 40 μm, the so-called size gap, in which neither condensational nor collisional growth is effective (e.g., Shaw, 2003; Devenish et al., 2012; Grabowski and Wang, 2013). Especially for droplet size distributions (DSDs) in a *colloidal stable* state (Squires, 1958), where collisions among droplets are inefficient due to a narrow DSD or too small droplets, mechanisms accelerating the collision-coalescence process to form a raindrop and initiate the precipitation are key to breaking this stability. Research over the past five decades has identified several key mechanisms: (i) DSD broadening by entrainment and mixing (Baker et al., 1980; Blyth, 1993; Krueger et al., 1997; Lasher-Trapp et al., 2005; Cooper et al., 2013; Hoffmann et al., 2019; Lim and Hoffmann, 2023), (ii) turbulence-induced collision enhancement (TICE), which increases the collision efficiency and reduces the size dependency of droplets to initiate collisions (e.g., Saffman and Turner, 1956; Kostinski and Shaw, 2005; Pinsky et al., 2008; Wang and Grabowski, 2009; Grabowski and Wang, 2013; Onishi et al., 2015; Hoffmann et al., 2017; Chen et al., 2020; Chandrakar et al., 2024), and (iii) the role of so-called precipitation embryos (PEs), the primary focus of this study.

The presence of PEs larger than 20 μm can initiate the collision process as they are already larger than the size-gap range (e.g., Woodcock, 1953; Telford, 1955; Johnson, 1982; Exton et al., 1986; Feingold et al., 1999; Teller and Levin, 2006; Alfonso

https://doi.org/10.5194/egusphere-2024-2636
Preprint. Discussion started: 29 August 2024

et al., 2013; Hoffmann et al., 2017; Dziekan et al., 2021). The sources of these PEs can be giant aerosol particles, predominantly large sea-salt aerosols that form solution droplets having a size range between 1 μm and 100 μm (Johnson, 1982; Blyth, 1993; O'Dowd et al., 1997; Feingold et al., 1999; Jensen and Nugent, 2017; Hudson and Noble, 2020; Hoffmann and Feingold, 2023), rare (one in a million) 'lucky' that grow faster than the average droplet and initiate precipitation (Telford, 1955; Kostinski and Shaw, 2005; Wilkinson, 2016; Alfonso and Raga, 2017; Alfonso et al., 2019), or particles from cloud seeding experiments to enhance precipitation (Bowen, 1952; Cotton, 1982).

Although the aforementioned studies generally agree that PEs can accelerate warm rain initiation, it is uncertain how their number and size affect the acceleration of droplet growth. Some studies suggest that a few 20 μm-sized droplets can effectively accelerate the rain initiation (e.g., Feingold et al., 1999) and change the amount of precipitation and cloud properties such as maximum droplet number concentration and liquid water content (e.g., Yin et al., 2000). Other studies indicate that the effectiveness of PEs relies on the type of the cloud, with shallower clouds being more susceptible (e.g., Kuba and Murakami, 2010; Dziekan et al., 2021). In particular, if we consider the stochastic fluctuations of the collision process, only a 12.5 μm-sized lucky droplet among 10 μm droplets can initiate collisions (Kostinski and Shaw, 2005). Thus, it is also important to account for stochastic fluctuations in the collision process. Lastly, although a few previous studies have investigated these mechanisms (Hoffmann et al., 2017; Chen et al., 2020), it remains unclear whether PE and TICE compete or complement each other in influencing collisional growth.

A particle-based Lagrangian cloud model (LCM) is the natural choice for such investigation (e.g., Gillespie, 1972; Shima et al., 2009; Hoffmann et al., 2017; Dziekan and Pawlowska, 2017; Unterstrasser et al., 2020; Li et al., 2022). Particularly, it was shown that a "one-to-one" LCM, where each computational particle represents one single cloud drop is suitable to consider stochastic fluctuations in collisional growth naturally (e.g., Dziekan and Pawlowska, 2017; Li et al., 2022). While considering the numerous processes that also affect warm rain initiation (i.e., aerosol activation and condensation) is essential for investigating rain initiation, a simple box model of the collision-coalescence process alone offers unique insights that cannot be captured in a more complex model due to its tremendous computational costs when using one-to-one LCM. Therefore, this study aims to investigate the early stages of collisional growth to determine the number and size of PEs needed to accelerate collisional growth.

This paper is organized as follows. Section 2 introduces the LCM box model and the simulation setup. Section 3 presents the results revealing the threshold on the minimum number and size of PEs to accelerate droplet collisions. Section 4 explores the mechanism behind the existence of this threshold. We conclude our paper in Sec. 6.

2 Model and Simulation Setup

2.1 Lagrangian Cloud Box Model

In most applications, each computational particle of an LCM represents a large number of real droplets with identical properties, frequently called superdroplets by introducing a weighting factor (W_i) (e.g., Shima et al., 2009). Thus, the number

https://doi.org/10.5194/egusphere-2024-2636
Preprint. Discussion started: 29 August 2024

concentration of droplets is determined by

$$N = \sum_{i=1}^{n_{\mathrm{ptcl}}} \frac{W_i}{\Delta V}, \tag{1}$$

where ΔV is a reference volume, and n_{ptcl} represents the number of computational particles in ΔV. In this study, we apply the "one-to-one" method, where each computational particle represents a single cloud droplet ($W_i = 1$). This approach fully captures the inherent stochasticity of the collision process (Shima et al., 2009; Dziekan and Pawlowska, 2017; Li et al., 2022).

The collision scheme follows the approach introduced by Shima et al. (2009) and Sölch and Kärcher (2010), in which a collision occurs with the probability

$$p_{m,n} = \frac{K}{\Delta V}\delta t, \tag{2}$$

primarily determined by the collection kernel

$$K = \pi(r_{\mathrm{m}} + r_{\mathrm{n}})^2 E(r_{\mathrm{m}}, r_{\mathrm{n}})|w(r_{\mathrm{m}}) - w(r_{\mathrm{n}})|, \tag{3}$$

where r_{m} and r_{n} are the radii of the interacting droplets, E the collision efficiency of droplet pairs (Hall, 1980), w the droplet terminal velocity (Beard, 1976), and δt the model time step. Here, we assume the coalescence efficiency to be unity. In this study, a collected droplet is removed from the simulation after the collision-coalescence event, and the mass of the collecting droplet increases by the mass of the collected droplet.

The simulations do not consider other processes besides collisional growth, such as condensation or sedimentation, which are beyond the focus of our study. Therefore, our results should be regarded as representative for the early stages of collisional growth only. For a detailed explanation of the LCM collision scheme, readers are referred to Hoffmann et al. (2017), Noh et al. (2018), and Unterstrasser et al. (2020).

2.2 Simulation Setups

The initial DSD is expressed as

$$N(m) = \frac{N_0}{\bar{m}} \exp\left(\frac{-m}{\bar{m}}\right), \tag{4}$$

where m is the mass of a droplet, $N_0 = 238\ \mathrm{cm}^{-3}$ the initial droplet number concentration, and $\bar{m}$ the mass of a droplet with $\bar{r} = 10$ µm (see orange line in Fig. 1). The DSD results in a cloud water mixing ratio (q_{c}) of approximately $1.0\ \mathrm{g\ kg}^{-1}$. Additionally, cases with $\bar{r} = 8,\ 12,$ or 14 µm are considered to investigate the effect of PEs in different DSD shapes. In these cases, $N_0 = 238,\ 456$ and $523\ \mathrm{cm}^{-3}$ to achieve the same $q_{\mathrm{c}} = 1.0\ \mathrm{g\ kg}^{-1}$ (Fig. 1). We name these cases 'RM', with the subsequent number denoting $\bar{r}$ (e.g., RM10).

To establish a *colloidally stable* initial DSD in which collisions are negligible, droplets larger than 20 µm are removed in selected simulations to prevent them from initiating collisions (Wang et al., 2006; Dziekan and Pawlowska, 2017); we will refer to such initialization as 'cut-off DSD,' (see dotted line in Fig. 1). In cases without this adjustment, where the initial DSD

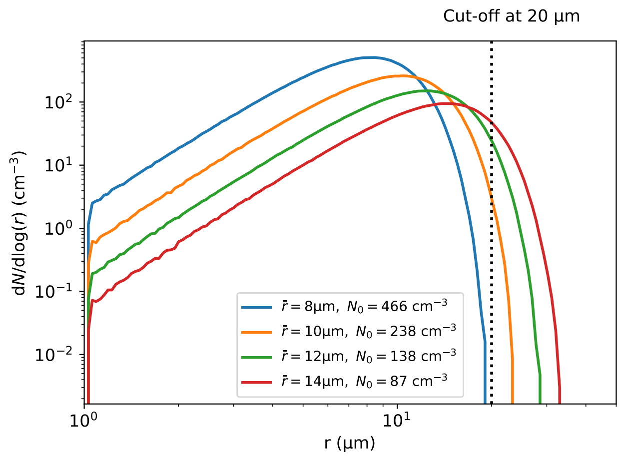

Figure 1. Initial DSDs for various $\bar{r}$ and corresponding N_0 values. The dotted line indicates the cut-off radius of 20 µm, above which droplets are removed in some cases.

is *broader*, we refer to it as the case with a *broad DSD* and denote it by adding the letter 'B' to the naming convention (e.g., RM10B). In this study, we primarily discuss the simulation with $\bar{r} = 10$ µm and cut-off DSD, i.e., the RM10 case, unless otherwise noted. Lastly, three different kinetic energy dissipation rates $\varepsilon = 16,\ 80,\ \text{and}\ 100\ \text{cm}^2\ \text{s}^{-3}$ are considered for RM10 case to investigate the effect of TICE. TICE is incorporated in Eq. 3 using the parameterizations developed by Ayala et al. (2008) and Wang and Grabowski (2009), which are steered by ε. When TICE is considered, the case names are amended by a T followed by the value of ε (e.g., RM10-T100).

A total of 10^6 computational particles ($n_{\text{ptcl}} = 10^6$) are initialized to represent the initial DSD resulting in a reference volume $\Delta V = 3.36 \times 10^{-3}\ \text{m}^3$. Every setup is simulated 100 times with different random numbers to ensure statistical convergence (cf. Fig. A1). Using a timestep $\delta t = 0.1$ s, the model is integrated for 7200 s to account for the slowest realization to complete collisional growth, but the discussion is focused on the initial 2500 s, capturing the initiation of collisional growth.

To explore the impact of PEs, we investigate 49 ensemble simulations, each representing different combinations of PE radii (r_{PE} = 15, 18, 22, 27, 33, 40, and 50 µm) and numbers (n_{PE} = 1, 3, 10, 30, 100, 300, and 1000). Here, we define PEs as any droplets added to the original DSD, although the conventional definition of PEs requires $r_{\text{PE}} > 20$ µm. The largest PE size is chosen to correspond to the size of haze particles grown from $1 - 5$ µm giant aerosols (Kuba and Murakami, 2010). We choose a minimum $n_{\text{PE}} = 1$ to investigate whether 'one in a million' lucky droplets could accelerate droplet collision, as highlighted in previous studies on lucky droplets (Kostinski and Shaw, 2005; Dziekan and Pawlowska, 2017). Maximum $n_{\text{PE}} = 1000$ is used for $r_{\text{PE}} = 15$ and 18 µm only, as larger PEs can substantially increase the initial q_c, limiting the comparability of the simulated cases. Within a given reference volume, the minimum and maximum n_{PE} can be interpreted as concentrations between $2.97 \times 10^{-4}\ \text{cm}^{-3}$ and $2.97 \times 10^{-1}\ \text{cm}^{-3}$, respectively.

In this study, the two specific timescales, t_{100} and $t_{10\%}$ are used to characterize precipitation efficiency. In previous studies, time for the first raindrop formation is used to quantify the efficiency of stochastic raindrop formation (Dziekan and Pawlowska,

https://doi.org/10.5194/egusphere-2024-2636
Preprint. Discussion started: 29 August 2024

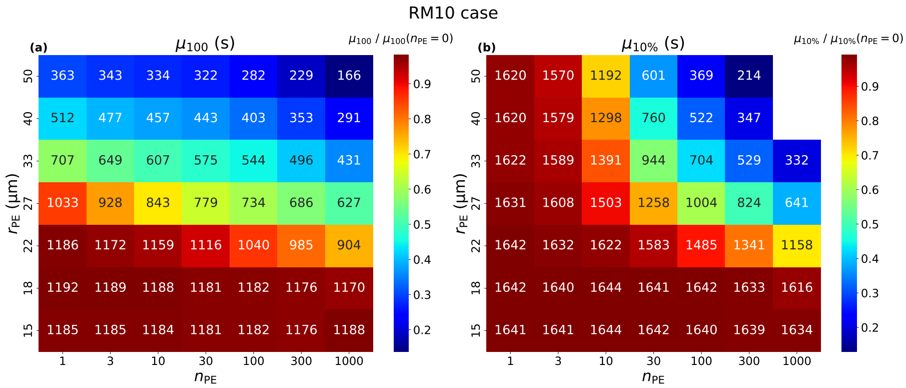

Figure 2. Ensemble-averaged values of (a) time for the first 100 µm raindrop formation, μ_{100}, (b) time for 10 % of cloud droplets to convert to raindrops, $\mu_{10\%}$, for RM10 case. The abscissa represents $n_{\rm PE}$, the ordinate represents $r_{\rm PE}$. The numbers in each box indicate the values of (a) μ_{100}, (b) $\mu_{10\%}$. $\mu_{10\%}$ values for $r_{\rm PE} \geq 40$µm and $n_{\rm PE} > 1000$ are not shown as the raindrop mass is already larger than 10 % due to large PEs. Colors in the plot represent the ratio of μ_{100} and $\mu_{10\%}$ to their values in the case without PEs ($n_{\rm PE} = 0$). In the case without PE, $\mu_{100} = 1214$ s, and $\mu_{10\%} = 1660$ s respectively.

2017). As PEs considered in this study can be larger than the typical raindrop radius, i.e., over 40 µm, we define t_{100} as the time required for the formation of the first 100 µm droplet, i.e., a sufficiently large droplet that stimulates subsequent collisions Kostinski and Shaw (2005); Alfonso et al. (2019). Thus, t_{100} characterized the efficiency for *raindrop formation*. The timescale $t_{10\%}$ represents the time when 10 % of the initial cloud droplet mass converts to rain, measuring the efficiency of *rain initiation* from a mass perspective (Onishi et al., 2015; Dziekan and Pawlowska, 2017).

3 PE Effect on Precipitation Timescales

3.1 Critical Thresholds for Raindrop Formation and Rain Initiation

Figure 2 shows the ensemble-averaged t_{100} and $t_{10\%}$, named μ_{100} and $\mu_{10\%}$, for RM10. In general, increasing $r_{\rm PE}$ and $n_{\rm PE}$ both shorten μ_{100} and $\mu_{10\%}$, indicating accelerated rain initiation. However, when $r_{\rm PE} \leq 18$ µm, i.e., smaller than the cut-off radius, μ_{100} and $\mu_{10\%}$ are not substantially accelerated compared to those cases without PEs regardless of $n_{\rm PE}$. Note that, in the case without PEs, μ_{100} and $\mu_{10\%}$ are 1213 s and 1660 s, respectively, for RM10. This indicates that the addition of PEs smaller than the maximum droplet radius of the DSD, even in large numbers (e.g., $n_{\rm PE} = 1000$), has a negligible effect on raindrop formation. Interestingly, for $\mu_{10\%}$, $n_{\rm PE}$ plays a more crucial rule than for the μ_{100}. For $n_{\rm PE} \leq 3$, $\mu_{10\%}$ is not accelerated (Fig. 2b) even for large PEs, whereas μ_{100} is accelerated (Fig. 2a). Thus, a faster μ_{100} does not always ensure a shorter $\mu_{10\%}$.

Overall, Fig. 2 shows μ_{100} and $\mu_{10\%}$ can be shortened with increasing $n_{\rm PE}$ and $r_{\rm PE}$, but only if a critical threshold is exceeded. Below this critical threshold, the effect of PEs on rain initiation is negligible. This raises the following question: What

https://doi.org/10.5194/egusphere-2024-2636
Preprint. Discussion started: 29 August 2024

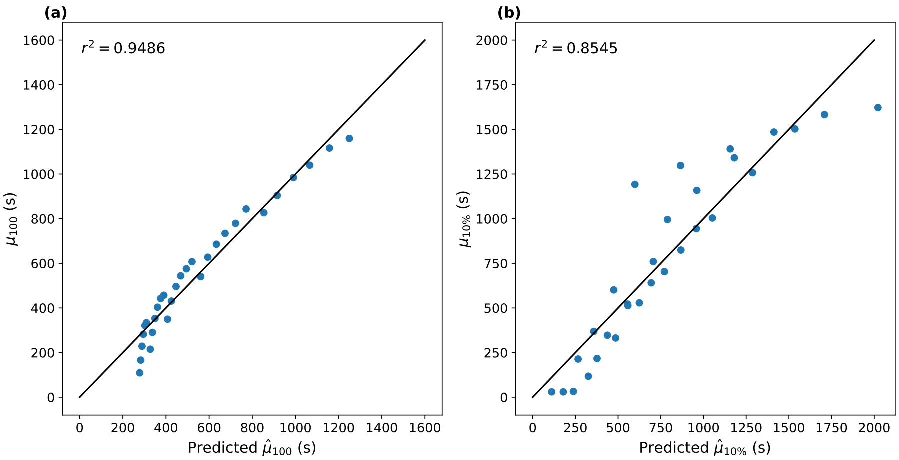

Figure 3. Scatter plots of simulated (a) μ_{100} and (b) $\mu_{10\%}$ (ordinate) and predicted values (abscissa) using Eq. (5) for RM10 case. Black solid lines indicate the one-to-one line.

are the specific size and number of PEs required to accelerate rain initiation substantially? To identify the critical threshold, we first express μ_{100} and $\mu_{10\%}$ as functions of n_{PE} and r_{PE}. As shown in Fig. 2, μ_{100} and $\mu_{10\%}$ are inversely related to the product of n_{PE} and r_{PE} once the critical threshold is exceeded. Thus, we write

$$\mu_\alpha = k_\alpha \Phi_\alpha(n_{\mathrm{PE}}, r_{\mathrm{PE}}) + c_\alpha = k_\alpha n_{\mathrm{PE}}^{-a_\alpha} r_{\mathrm{PE}}^{-b_\alpha} + c_\alpha \tag{5}$$

for a μ_α exceed the critical threshold. Here k_α is a rate-of-change coefficient, c_α a constant, $\Phi_\alpha(n_{\mathrm{PE}}, r_{\mathrm{PE}})$ represents the composite relationship of n_{PE} and r_{PE} with scaling exponets a_α and b_α, and the subscript α is 100 or 10% for μ_{100} and $\mu_{10\%}$, respectively.

To determine the parameters of Eq. (5), we fit a_α, b_α, c_α, and k_α, using μ_{100} and $\mu_{10\%}$ from cases with $r_{\mathrm{PE}} \geq 22$ and $n_{\mathrm{PE}} \geq 10$. In these cases, both μ_{100} and $\mu_{10\%}$ are directly affected by changes in r_{PE} and n_{PE} (Fig. 2), i.e., the PE critical threshold is exceeded. The fitted parameters are $a_{100} = 0.086$, $b_{100} = 3.086$, $c_{100} = 244$ s, and $k_{100} = 17308248$ for μ_{100}, and $a_{10\%} = 0.13$, $b_{10\%} = 1.13$, $c_{10\%} = -310$ s, and $k_{10\%} = 104016$ for $\mu_{10\%}$ with r_{PE} in µm. Note that, while units of each parameter are detailed in Appendix B, our focus will be on $\Phi_\alpha(n_{\mathrm{PE}}, r_{\mathrm{PE}}$, i.e., a_α and b_α first. The parameters c_α and k_α will be discussed in more detail after we expand Eq. (5) with more physically meaningful terms. The values of a_α and b_α indicate that both μ_{100} and $\mu_{10\%}$ are more sensitive to r_{PE} than n_{PE}. When comparing a_{100} and b_{100} to $a_{10\%}$ and $b_{10\%}$, $\mu_{10\%}$ seems to depend more on n_{PE} and less on r_{PE}, than μ_{100}, which is consistent with the results shown in Fig. 2. Figure 3 juxtaposes the simulated and predicted μ_{100} and $\mu_{10\%}$ values using Eq. (5). This result indicates that μ_{100} and $\mu_{10\%}$ can be expressed with Φ_α relatively well. However, Eq. (5) tends to overestimate $\mu_{10\%}$ when it is below 750 s, and generally fails to predict $\mu_{10\%}$ when it is over 1000 s (Fig. 3b). This is due to the cases with $n_{\mathrm{PE}} < 10$ and $r_{\mathrm{PE}} < 22$ µm, which show almost no dependency on r_{PE}.

https://doi.org/10.5194/egusphere-2024-2636
Preprint. Discussion started: 29 August 2024

To better capture the behavior of μ_{100} and $\mu_{10\%}$, especially near the critical threshold where the dependency on r_{PE} and n_{PE} vanishes, we expand Eq. (5) by a Heaviside step function $\mathcal{H}$, such that

$$\mu_\alpha(\Phi) = \mu_{\alpha,\mathrm{c}} - k_\alpha(\Phi_{\alpha,\mathrm{c}} - \Phi_\alpha) \cdot \mathcal{H}(\Phi_{\alpha,\mathrm{c}} - \Phi_\alpha), \tag{6}$$

where $\mu_{\alpha,\mathrm{c}}$ is the baseline value of μ_α in the absence of PEs incorporating parameter c_α from above. When fitting Eq. (6) all results, including cases where $r_{\mathrm{PE}} < 22$ and $n_{\mathrm{PE}} < 10$, are used, with parameters a_α and b_α fixed to the values obtained previously. The specific parameters for Eq. (6) and their r-squared values are detailed in Appendix B. In general, r-squared values exceed 0.95 for μ_{100}, and range from 0.75 to 0.9 for $\mu_{10\%}$. The results of $\mu_{100}(\Phi)$ and $\mu_{10\%}(\Phi)$ for the RM10 case are shown in Fig. 4a and b as blue solid lines. Until exceeding the critical thresholds ($\Phi_{100,\mathrm{c}} = 5.04 \times 10^{-5}$ and $\Phi_{10\%,\mathrm{c}} = 1.51 \times 10^{-2}$; see Tabs. B1 and B2), μ_{100} and $\mu_{10\%}$ remain constant at $\mu_{100,\mathrm{c}} = 1190$ s and $\mu_{10\%,\mathrm{c}} = 1608$ s. These values agree well with μ_{100} and $\mu_{10\%}$ without PEs, 1214 s and 1660 s, respectively. However, once Φ_α becomes smaller than $\Phi_{\alpha,\mathrm{c}}$, i.e., exceeds the critical threshold, μ_{100} and $\mu_{10\%}$ decrease as expected from Eq. (5).

3.2 Factors Controlling the Critical Threshold

Using Eq. (6), we are now able to investigate how the critical threshold varies for different initial DSD shapes (characterized by $\bar{r}$ and the consideration of a cut-off radius) and the presence of TICE. To achieve this, we fit the results to Eq. (6) for RM8, RM10, RM12, and RM14 with or without cut-off DSD (Fig. 4a, b, c, and d). Additionally, we consider TICE for RM10 (Fig. 4e and f). Although a_α and b_α parameters for Φ_{100} and $\Phi_{10\%}$ may vary for different cases, we fix them to the values obtained earlier (see Fig. 3) to directly compare $\mu_{\alpha,\mathrm{c}}$, $\Phi_{\alpha,\mathrm{c}}$ and k_α across different initial conditions. The fitted parameters for these initial conditions are detailed in Appendix B. Figure 4 shows that all cases exhibit the same fundamental feature: the presence of a critical threshold $\Phi_{\alpha,\mathrm{c}}$.

We first discuss the results for μ_{100}. As $\bar{r}$ increases, $\mu_{100,\mathrm{c}}$ decreases (Figs. 4a and 5b), indicating that it takes less time to produce a large raindrop even without PEs. This is due to the increased number of large droplets when $\bar{r}$ increases, although the largest droplet size remains unchanged due to the cut-off DSD. In this case, $\Phi_{100,\mathrm{c}}$ also decreases with increasing $\bar{r}$, implying more and larger PEs are needed to exceed the critical threshold (Fig. 5a).

Results from the cases with a broad DSD with different $\bar{r}$ are shown in Fig. 4c and d. In these cases, also the maximum radius of the droplet and hence the DSD width increases, making droplet collisional growth more efficient (cf. Fig. 4a and b). For the same $\bar{r}$, we see that $\Phi_{100,\mathrm{c}}$ is smaller in broad DSD cases (Fig. 5a). This is because of the presence of larger droplets in the initial DSD, which are equally efficient as PEs in the collision process, reducing the importance of the PE effect. Moreover, both $\mu_{100,\mathrm{c}}$ and $\Phi_{100,\mathrm{c}}$ decrease with increasing $\bar{r}$ (Fig. 4c and d and Fig. 5a). This is because, without cut-off DSD, both the size and the number of large droplets increase with increasing $\bar{r}$, (cf. Fig. 1). The results for $\mu_{10\%,\mathrm{c}}$ and $\Phi_{10\%,\mathrm{c}}$ show a similar pattern to those of $\mu_{100,\mathrm{c}}$ and $\Phi_{100,\mathrm{c}}$ (Fig. 4c and Fig. 5c and d), where both $\mu_{10\%,\mathrm{c}}$ and $\Phi_{10\%,\mathrm{c}}$ decrease with increasing $\bar{r}$ in the absence of the cut-off DSD .

Additionally, the TICE effect is considered for RM10 (Fig. 4e and f). TICE is considered with three different $\varepsilon = 16$, 80 and 100 $\mathrm{cm}^2\,\mathrm{s}^{-3}$ which are typically found within different cloud types: $1 - 10$ $\mathrm{cm}^2\,\mathrm{s}^{-3}$ in stratocumulus clouds, $10 - 100$ $\mathrm{cm}^2\,\mathrm{s}^{-3}$ in shallow

https://doi.org/10.5194/egusphere-2024-2636
Preprint. Discussion started: 29 August 2024

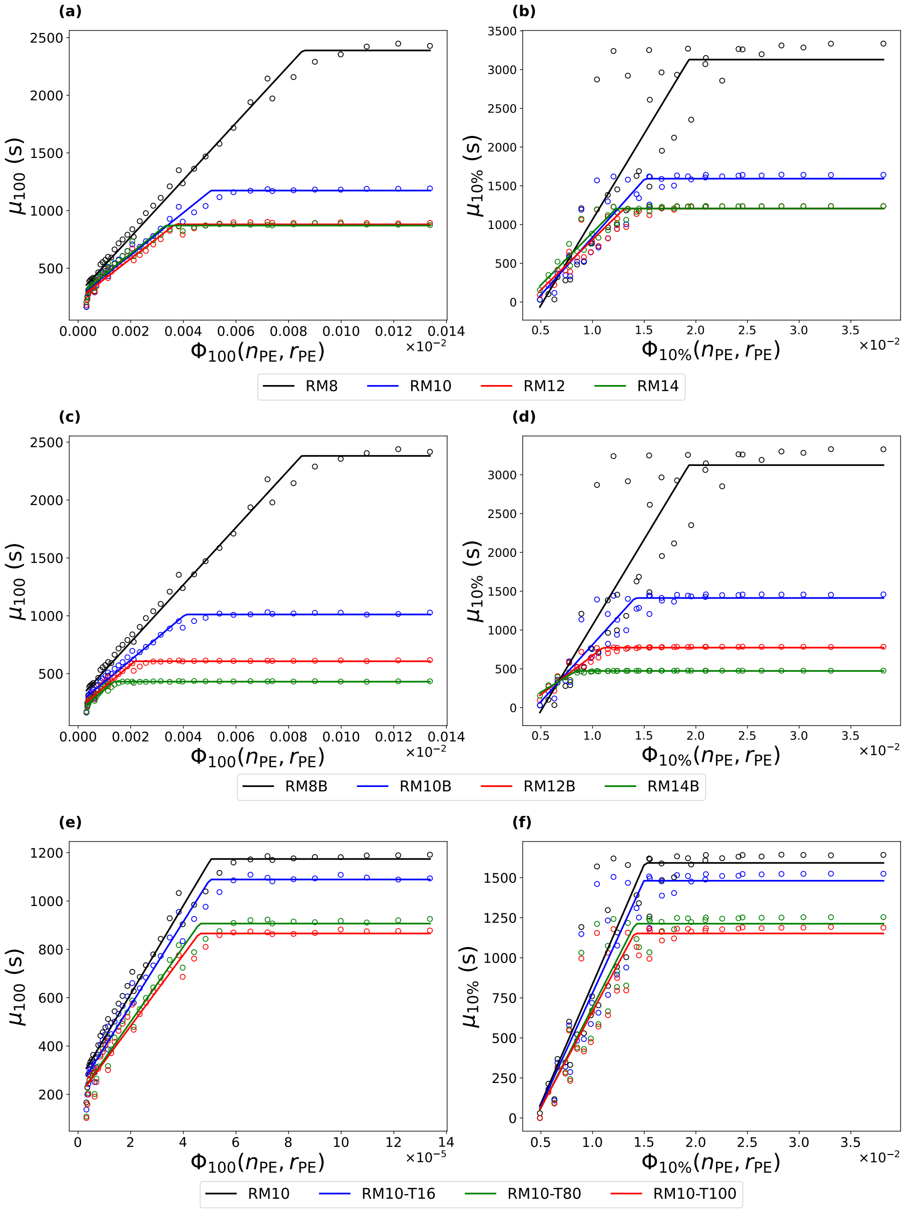

Figure 4. μ_{100} (left column) and $\mu_{10\%}$ (right column) as a function of Φ_α for different initial conditions are shown. Each point represents the simulation results, while solid lines indicate the fitted Eq. (6). The first row (a and b) represents cases with cut-off DSD (RM8, RM10, RM12, and RM14), and the second row (c and d) represents cases without cut-off DSD (RM8B, RM10B, RM12B, and RM14B). The third row (e and f) represents RM10 with different ε values (RM10-T16, RM10-T80, and RM10-T100).

convective clouds, and $100 - 1000\ \mathrm{cm^2\ s^{-3}}$ in deep convective clouds (Siebert et al., 2006; Seifert et al., 2010; Pruppacher and Klett, 2012). With strong turbulence ($\varepsilon = 80 - 100\ \mathrm{cm^2\ s^{-3}}$), $\Phi_{100,c}$ is lower (Figs. 4a and 5a) than in the case with no or

https://doi.org/10.5194/egusphere-2024-2636
Preprint. Discussion started: 29 August 2024

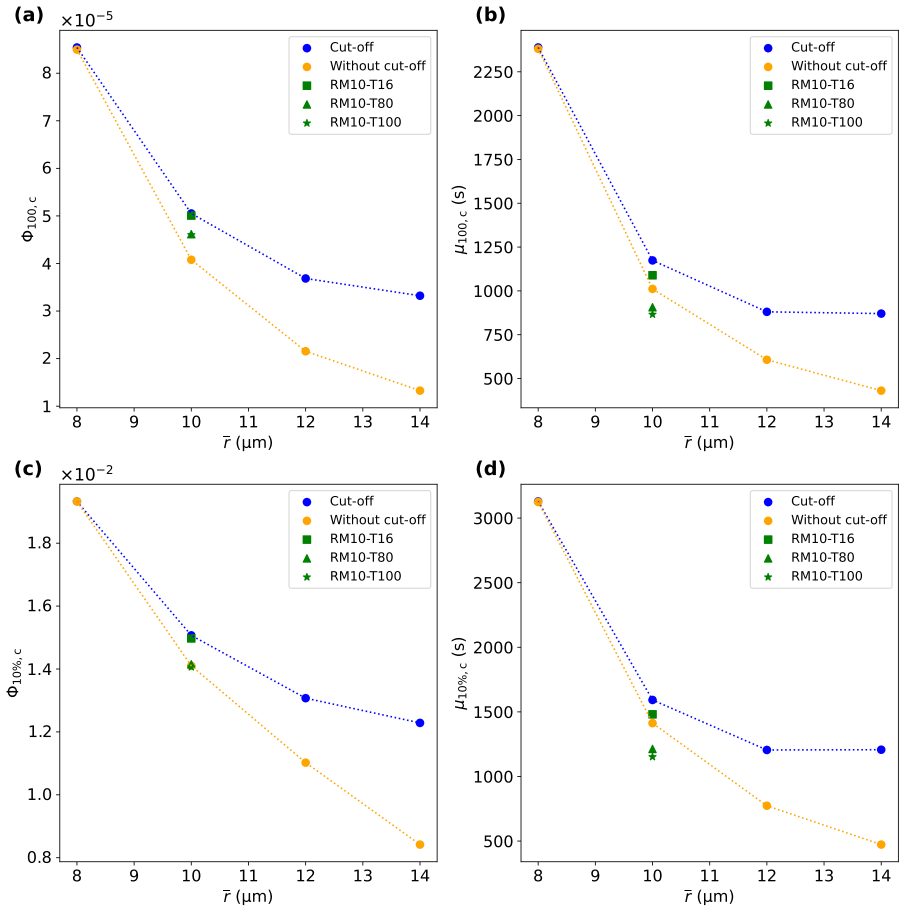

Figure 5. Results of (a) $\Phi_{100,\mathrm{c}}$, (b) $\mu_{100,\mathrm{c}}$, (c) $\Phi_{10\%,\mathrm{c}}$ and (d) $\mu_{10\%,\mathrm{c}}$ for different $\bar{r}$. Blue circles depict the cases with cut-off DSD while orange circles depict cases without cut-off DSD. Green square, triangle, and star shape represent the results with $\varepsilon = 16,\ 80,\ 100\ \mathrm{cm^2\ s^{-3}}$, respectively, for the RM10 case.

weaker TICE ($\varepsilon = 16\ \mathrm{cm^2\ s^{-3}}$). Thus, more and larger PEs are required to substantially accelerate μ_{100} with TICE. In other words, the PE effect becomes weaker when TICE is strong. Both $\Phi_{100,\mathrm{c}}$ and $\Phi_{10\%,\mathrm{c}}$ decrease but only slightly with TICE but they never fall below the values observed in the broad DSD case (Fig. 5a and c). In contrast, $\mu_{100,\mathrm{c}}$ and $\mu_{10\%,\mathrm{c}}$ decrease more substantially with increasing ε, becoming even shorter than in the broad DSD case (Fig. 5b and d). This suggests that TICE enhances the efficiency of every collision event, leading to a faster $\mu_{10\%,\mathrm{c}}$, due to collisions among all cloud droplets in the entire system. However, the impact of TICE on the critical threshold is less pronounced than that of the DSD shape ($\bar{r}$ and cut-off DSD).

In summary, when droplet collisions are efficient without PEs, whether due to a large $\bar{r}$, the presence of large droplets (i.e., broad DSD), or TICE, the PE size and number needs to be larger to accelerate rain initiation substantially. Although we have identified the existence of the critical threshold, there remains uncertainty regarding why $t_{10\%}$ is not always shorter than

https://doi.org/10.5194/egusphere-2024-2636
Preprint. Discussion started: 29 August 2024

the case without PEs when n_{PE} is small, even though t_{100} is decreased (e.g., $n_{\mathrm{PE}} < 10$ cases in Fig. 2). This discrepancy may arise because $t_{10\%}$ involves interactions among multiple droplets and PEs, whereas t_{100} depends on the behavior of an individual droplet or PEs. This suggests that while PEs can accelerate the formation of the largest raindrop, these droplets may not substantially impact the overall rain initiation after the initial period when they are few. This contradicts the 'lucky droplet' theory that a few lucky droplets trigger the subsequent runaway growth and rain initiation (Kostinski and Shaw, 2005; Alfonso and Raga, 2017). In the following section, we will explore how PEs affect $t_{10\%}$ to explain why a shorter t_{100} does not ensure a shorter $t_{10\%}$.

4 PE Effects on Rain Initiation

In order to understand the effects of PE size and number on rain initiation more clearly, we consider the time series of raindrop mixing ratio q_{r}, autoconversion rate (i.e., raindrop formation by collisions between cloud droplets), and accretion rate (i.e., raindrop growth by raindrops collecting cloud droplets) using $r_{\mathrm{PE}} = 22$ µm and 27 µm with different n_{PE} ranging from 0 to 300 for RM10 (Fig. 6). Overall, q_{r} evolves faster for larger r_{PE} and n_{PE} (Fig. 6a and b). However, with PEs below the critical threshold (i.e., for $n_{\mathrm{PE}} \leq 30$ at $r_{\mathrm{PE}} = 22$ µm and $n_{\mathrm{PE}} \leq 3$ at $r_{\mathrm{PE}} = 27$ µm), the difference from the case with and without PE is insignificant, implying that PEs do not substantially enhance rain initiation, although raindrop formation ($q_r > 0$) starts earlier (Fig. 6a and b). This result is consistent with Fig. 2, in which μ_{100} is smaller than $\mu_{100,\mathrm{c}}$, but $\mu_{10\%}$ is comparable to $\mu_{10\%,\mathrm{c}}$.

The time series of autoconversion and accretion evolution provides more details on how PEs affect rain initiation. In Fig. 6c to f, solid lines represent droplet growth without PEs (i.e., between non-PE droplets exclusively), while dotted lines represent droplet growth involving PEs (i.e., collisions between PEs and non-PE droplets or among PEs). We found that non-PE autoconversion decreases with increasing n_{PE} (Fig. 6c and d). This is because large PEs have an advantage in the autoconversion process, growing faster and collecting non-PE droplets, which in turn suppresses the autoconversion of non-PE droplets.

For $r_{\mathrm{PE}} = 22$ µm, both autoconversion and accretion initiate earlier with PEs than in the case without PEs, but only when $n_{\mathrm{PE}} \geq 100$ (Fig. 6c). When $n_{\mathrm{PE}} < 30$, autoconversion and consequently accretion by PEs are even slower than those of non-PE droplets. This is because autoconversion depends heavily on stochastic events. Thus although larger PEs are more likely to collide, a small n_{PE} reduces the likelihood of these collisions, making PE autoconversion slower than non-PE autoconversion. Thus, when n_{PE} is small, PEs may not decrease $t_{10\%}$, although t_{100} can be shorter than in the cases without PEs.

For $r_{\mathrm{PE}} = 27$ µm, while non-PE-autoconversion always decreases with increasing n_{PE}, PE-autoconversion increases substantially only when $n_{\mathrm{PE}} \geq 100$. Therefore, before exceeding the critical threshold, PEs suppress non-PE autoconversion more than they enhance autoconversion which can even lead to a decrease in the total (PE and non-PE) autoconversion. Interestingly, in this case, the time to initiate PE autoconversion remains unchanged with n_{PE} affecting only its magnitude (Fig. 6c). The initiation time for PE autoconversion is influenced by r_{PE} since this process is closely related to the number of collisions or time required for droplets to grow larger than 40 µm, which occurs more quickly for larger PEs (cf. Fig. 6c and d). Thus, r_{PE}

https://doi.org/10.5194/egusphere-2024-2636
Preprint. Discussion started: 29 August 2024

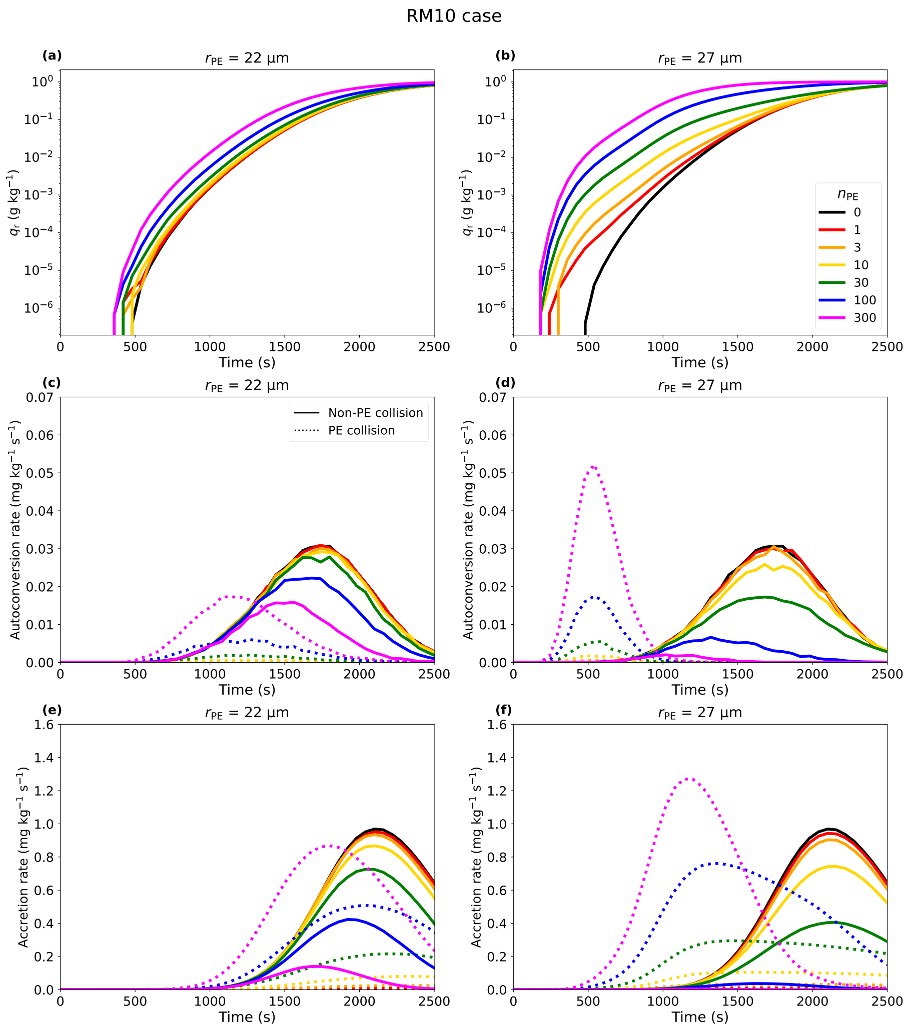

Figure 6. Time series of (a/b) raindrop mixing ratio, (c/d) autoconversion rate, and (e/f) accretion rate, for the RM10 case, shown for two different values of r_{PE}: 22 µm (first column) and 27 µm (second column). The colors of the lines represent different n_{PE} values, with the black solid line representing the result from the simulation without PEs ($n_{\mathrm{PE}} = 0$). In (c) to (f), the solid lines denote autoconversion and accretion without PEs (between non-PE droplets exclusively), while the dotted line depicts autoconversion and accretion by PEs.

determines the initiation time for autoconversion, especially when $r_{\mathrm{PE}} \geq 27$ µm, while n_{PE} determines how much non-PE droplet autoconversion and accretion are suppressed.

Accretion starts earlier when $r_{\mathrm{PE}} = 22$ µm and $n_{\mathrm{PE}} > 100$ and any n_{PE} for $r_{\mathrm{PE}} = 27$ µm (Fig. 6e and f), which is triggered by the earlier raindrop formation by autoconversion (Fig. 6c and d). However, even for $r_{\mathrm{PE}} = 27$ µm, accretion by PEs increases only slightly when $n_{\mathrm{PE}} \leq 30$, i.e., below the critical threshold. Once the critical threshold is exceeded, particularly for n_{PE}, accretion is substantially increased and accelerated compared to the case for $n_{\mathrm{PE}} = 0$ (Fig. 6e and f). In this case, accretion is

https://doi.org/10.5194/egusphere-2024-2636
Preprint. Discussion started: 29 August 2024

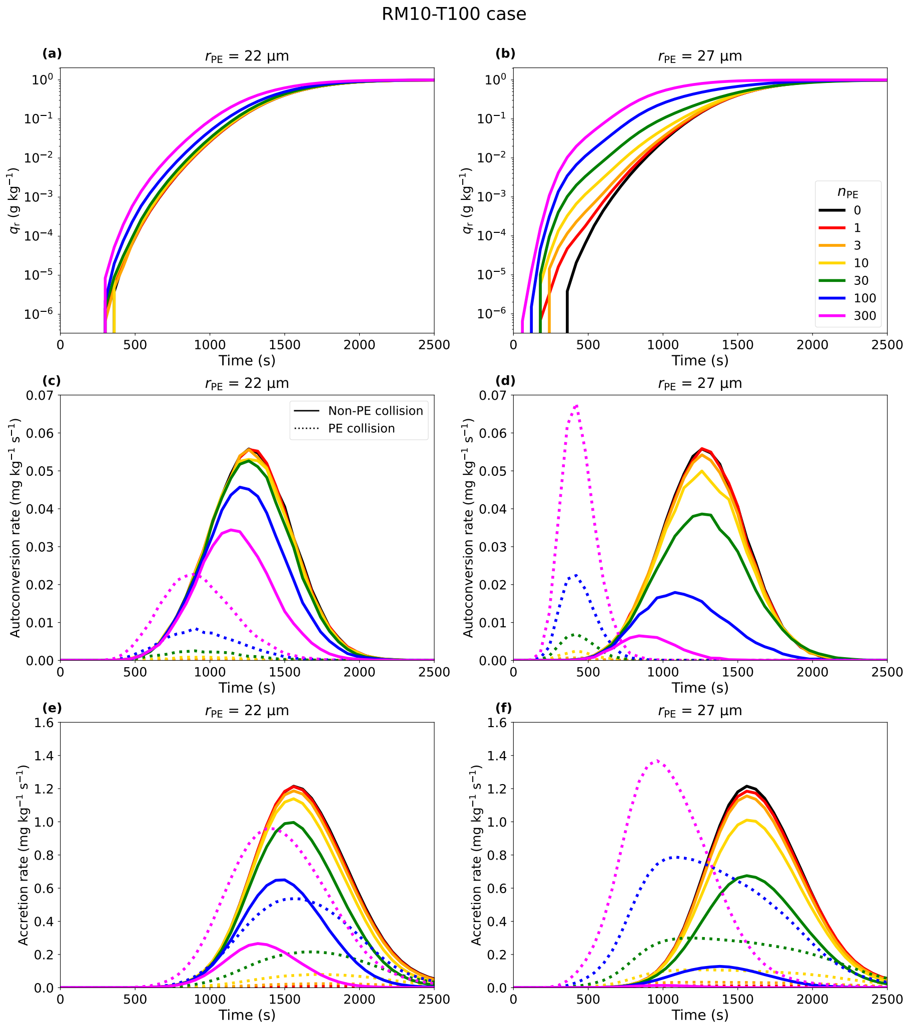

Figure 7. Same as for Fig. 6 but for cases with $\varepsilon = 100\ \mathrm{cm^2\ s^{-3}}$.

dominated by PEs, outweighing the decrease in non-PE autoconversion (Fig. 6e and f), and initially larger q_r persists (Fig. 6a and b).

Results with TICE ($\varepsilon = 100\ \mathrm{cm^2\ s^{-3}}$, Fig. 7) also highlight the importance of PEs in suppressing non-PE autoconversion. With TICE, collisions between small and similar-sized droplets are more efficient (Pinsky et al., 2008). Thus, with TICE, non-PE autoconversion is still substantial when $n_\mathrm{PE} = 100$ (blue and purple solid lines in Fig. 7b), while it is almost totally suppressed without TICE (blue and purple solid lines in Fig. 6d). Thus, more and larger PEs are needed to outweigh non-PE accretion, making droplet growth less sensitive to PEs when TICE is considered. However, even with TICE, if n_PE substantially exceeds the critical threshold ($r_\mathrm{PE} = 27$ µm and $n_\mathrm{PE} = 300$), droplet collisional growth is entirely dominated by PEs (purple

https://doi.org/10.5194/egusphere-2024-2636
Preprint. Discussion started: 29 August 2024

solid line in Fig. 7f). Thus, while both PEs and TICE accelerate droplet collisional growth, each effect becomes weaker when the other effect dominates rain initiation (e.g., Chandrakar et al., 2024).

5 Summary and Conclusion

Understanding whether precipitation embryos (PEs), particles larger than the so-called size gap range, can accelerate the droplet collision process remains a key question in warm rain initiation. Despite decades of research on the effect of PEs on rain initiation (e.g., Telford, 1955; Johnson, 1982; Feingold et al., 1999; Teller and Levin, 2006; Alfonso et al., 2013), this challenge persists and is still highlighted in recent studies (e.g., Chen et al., 2020; Dziekan et al., 2021; Chandrakar et al., 2024), underscoring the need for further investigation.

In this study, we systematically investigated how PEs affect droplet collisional growth using ensembles of Lagrangian cloud model (LCM) collision simulations. Our primary focus was to identify the minimal PE size and number necessary to accelerate the droplet collision-coalescence process substantially. We evaluated the droplet collision efficiency using two timescales: the time required for the first 100 μm droplet to form (t_{100}) and the time to convert 10% of the total initial cloud mass to rain mass ($t_{10\%}$).

We found that the droplet collision process does not substantially accelerate when the number or size of PEs is below a critical threshold. t_{100} is accelerated only when the radii of PEs are larger than the maximum droplet radius of non-PE droplets. This is because t_{100} is more related to the growth of a single droplet where larger droplets, such as PEs, are expected to grow faster than smaller droplets. In contrast, $t_{10\%}$ depends more on the number of PEs. Even with substantially large PEs, a faster formation of the first large raindrop does not always ensure faster rain initiation when the number of PEs is small. This is because PEs increase autoconversion and accretion only when their number is sufficient while simultaneously suppressing the autoconversion of non-PE droplets to become raindrops. Thus, when autoconversion of non-PE droplets is already efficient, more or larger PEs are required to accelerate $t_{10\%}$.

To determine the critical threshold for rain initiation by PEs, we derived a simple equation that relates the number and size of PEs to t_{100} and $t_{10\%}$. The equation revealed that the critical threshold depends on the colloidal stability of the droplet size distribution (DSD) characterized by the DSD shape or turbulence-induced collision enhancement (TICE). We showed that increasing the droplet mean radius and hence the size of pre-existing large droplets decreases the colloidal stability of DSD and makes the collisional process less susceptible to PE perturbations because non-PE droplet collisions are already sufficient for initiating rain. Equivalently, more and larger PEs are needed to substantially accelerate the droplet growth with TICE, which increases the collision frequency among smaller non-PE droplets making the collision process less reliant on PEs.

While PEs can accelerate the rain initiation by collecting other droplets, they may reduce the number of raindrops by suppressing non-PE droplets to grow as raindrops. As a result, clouds without PEs may have more and larger raindrops, as PEs do not collect those before reaching the cloud top. This might lead to longer-lasting clouds and affect the precipitation differently. Thus, validating this study's findings in more complex scenarios is mandatory, for the future. These should incorporate additional processes such as aerosol activation, condensation, entrainment, and especially, collisional droplet breakup (Low

https://doi.org/10.5194/egusphere-2024-2636
Preprint. Discussion started: 29 August 2024

and List, 1982) which increases the small number of PEs, causing more PE accretion afterward or droplet sedimentation which decreases the effect of PEs by making large raindrops precipitate and prevents PEs from further collisions

In conclusion, we confirm that a DSD barely producing raindrops is more sensitive to PEs (e.g., Dziekan et al., 2021). This underscores the need for caution in geoengineering approaches like marine cloud brightening (Latham et al., 2012), aiming to create highly reflective clouds by artificially adding aerosol particles, where the unintended initiation of rain by adding large particles could be counterproductive (Hoffmann and Feingold, 2021). Indeed, this study found that PEs surpassing a critical threshold can initiate rain, while numerous PEs with a sufficiently small size are harmless. In addition, approaches to enhance precipitation, such as cloud seeding (Bowen, 1952; Cotton, 1982), should prioritize identifying target clouds with high stability and minimal rain production to maximize efficiency.

Code and data availability. A Python version of the LCM code is available on the link (https://github.com/jslim93/PyLCM_edu). The simulations were conducted using the FORTRAN version of the code, which employs the same collision routine as the Python version but provides faster computation. Simulation data will be made available upon request to the authors.

Appendix A: Ensemble Size Sensitivity of t_{100} and $t_{10\%}$

Figure A1 illustrates how the mean and standard deviation of t_{100} (μ_{100} and σ_{100}, respectively) and $t_{10\%}$ ($\mu_{10\%}$ and $\sigma_{10\%}$, respectively) evolve as the ensemble size increases from 1 to 200 for RM10 without PEs ($n_{\mathrm{PE}} = 0$). The mean values and standard deviations begin to converge when the ensemble size exceeds 100. Therefore, we consider an ensemble size of 100 adequate for obtaining reliable results.

https://doi.org/10.5194/egusphere-2024-2636
Preprint. Discussion started: 29 August 2024

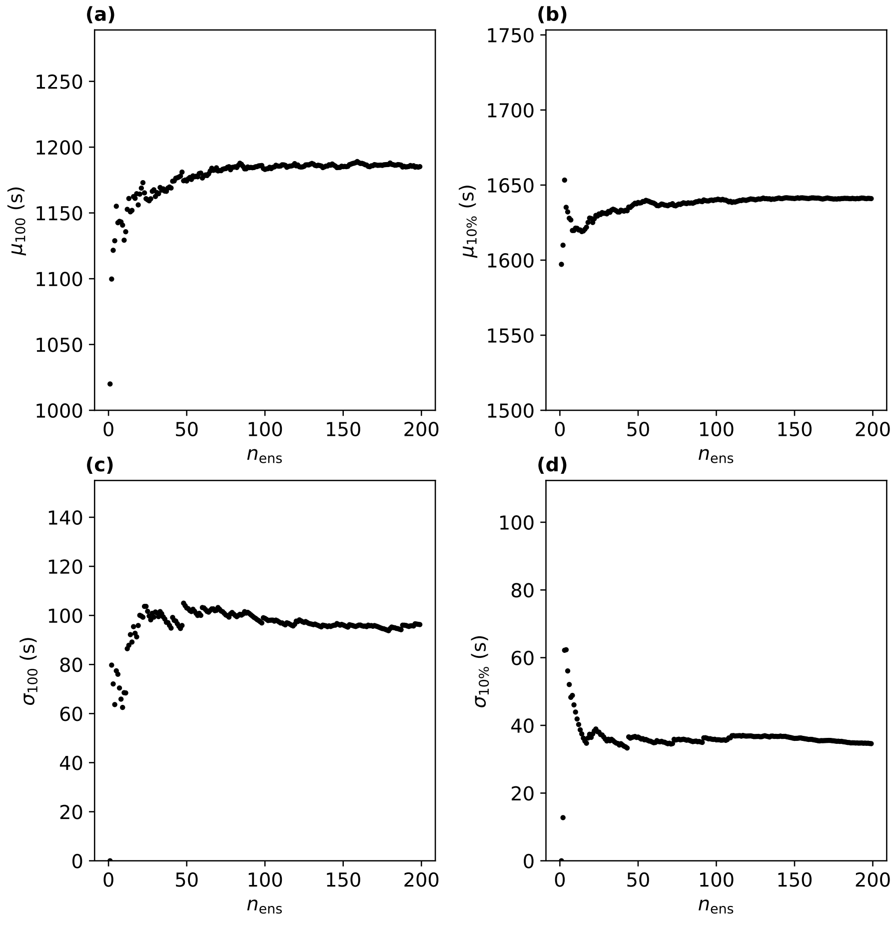

Figure A1. Variation of (a) μ_{100}, (b) $\mu_{10\%}$, (c) σ_{100} and (d) $\sigma_{10\%}$ with ensemble size ($n_{\rm ens}$) for RM10 case and without PEs ($n_{\rm PE} = 0$).

https://doi.org/10.5194/egusphere-2024-2636
Preprint. Discussion started: 29 August 2024

Appendix B: Parameters for the Fitting Function

Table B1 depicts the parameters and r^2 values derived from curve fitting Eq. (6) to μ_{100} for each result shown in Fig. 4a. Similarly, Table B2 shows the parameters and the r^2 values obtained from fitting Eq. (6) to $\mu_{10\%}$ for the results shown in Fig. 4b. The naming conventions for each case are as follows: Numbers following ‘RM’ denote $\bar{r}$ (e.g., ‘RM8’ corresponds to cases with $\bar{r} = 8$ µm). ‘B’ denotes cases without cut-off DSD. Numbers following ‘T’ indicate ε (e.g., T16 corresponds to cases with $\varepsilon = 16\ \mathrm{cm}^2\,\mathrm{s}^{-3}$). The units of $\mu_{100,\mathrm{c}}$ and $\mu_{10\%,c}$ are in s, Φ_{100} in µm$^{-1.852}$ and $\Phi_{10\%}$ in µm$^{-6.78}$. Units of Φ_{100} and $\Phi_{10\%}$ are determined by Eq. 5 with respective a_α, b_α parameters, where the unit of r_{PE} is µm and n_{PE} is unit-less. The subscript α is 100 or 10% for μ_{100} and $\mu_{10\%}$, respectively. Thus, the units of k_α for μ_{100} and $\mu_{10\%}$ are µm$^{1.852}$ s and µm$^{6.78}$ s, respectively. In this study, these parameters are mainly used to compare how critical threshold varies in different cases than to obtain actual values.

https://doi.org/10.5194/egusphere-2024-2636
Preprint. Discussion started: 29 August 2024

Table B1. Parameters for fitting function of μ_{100}

	RM8	RM10	RM12	RM14	RM8B
$\Phi_{100,c}$	8.54×10^{-5}	5.05×10^{-5}	3.69×10^{-5}	3.32×10^{-5}	8.50×10^{-5}
$\mu_{100,c}$	2388.73	1173.81	880.46	870.40	2381.12
k_{100}	2.47×10^{7}	1.83×10^{7}	1.77×10^{7}	1.85×10^{7}	2.48×10^{7}
r^2	0.99	0.98	0.98	0.97	0.99

	RM10B	RM12B	RM14B	RM10-T16	RM10-T80	RM10-T100
$\Phi_{100,c}$	4.08×10^{-5}	2.16×10^{-5}	1.33×10^{-5}	5.01×10^{-5}	4.62×10^{-5}	4.60×10^{-5}
$\mu_{100,c}$	1011.30	607.01	430.81	1089.05	906.69	865.67
k_{100}	1.89×10^{7}	1.92×10^{7}	2.05×10^{7}	1.73×10^{7}	1.55×10^{7}	1.47×10^{7}
r^2	0.98	0.97	0.95	0.98	0.97	0.97

https://doi.org/10.5194/egusphere-2024-2636
Preprint. Discussion started: 29 August 2024

Table B2. Parameters for fitting function of $\mu_{10\%}$

	RM8	RM10	RM12	RM14	RM8B
$\Phi_{10\%,c}$	1.93×10^{-2}	1.51×10^{-2}	1.31×10^{-2}	1.23×10^{-2}	1.93×10^{-2}
$\mu_{10\%,c}$	3128.99	1592.18	1205.14	1207.07	3124.57
$k_{10\%}$	2.21×10^{5}	1.49×10^{5}	1.30×10^{5}	1.35×10^{5}	2.21×10^{5}
r^2	0.78	0.85	0.89	0.90	0.78

	RM10B	RM12B	RM14B	RM10-T16	RM10-T80	RM10-T100
$\Phi_{10\%,c}$	1.41×10^{-2}	1.10×10^{-2}	8.42×10^{-3}	1.50×10^{-2}	1.41×10^{-2}	1.41×10^{-2}
$\mu_{10\%,c}$	1412.81	773.39	472.91	1480.90	1212.93	1151.98
$k_{10\%}$	1.47×10^{5}	1.00×10^{5}	8.00×10^{4}	1.41×10^{5}	1.26×10^{5}	1.20×10^{5}
r^2	0.87	0.92	0.91	0.85	0.85	0.85

Author contributions. JSL, YN, HL, and FH conceived the original conceptualization and interpretation of results and contributed to discussions. FH provided the base model and JSL modified the base model and formally analyzed the results. JSL wrote the original draft and JSL, YN, FH, and HL contributed to the review and editing. YN and FH provided the funding acquisition for the study and project administration.

Competing interests. There are no competing interests.

Acknowledgements. This work was supported by the Korea Meteorological Administration Research and Development Program under grant KMI2021-01512, the National Research Foundation of Korea (NRF) grant funded by the Korean government (MSIT) (2021R1F1A1051121), and the Emmy-Noether Program of the German Research Foundation (DFG) under grant HO 6588/1-1. The authors gratefully acknowledge the Gauss Centre for Supercomputing e.V. (www.gauss-centre.eu) for funding this project by providing computing time on the GCS Supercomputer SuperMUC-NG at Leibniz Supercomputing Centre (www.lrz.de).

https://doi.org/10.5194/egusphere-2024-2636
Preprint. Discussion started: 29 August 2024

References

Alfonso, L. and Raga, G. B.: The impact of fluctuations and correlations in droplet growth by collision–coalescence revisited–Part 1: Numerical calculation of post-gel droplet size distribution, Atmospheric Chemistry and Physics, 17, 6895–6905, https://doi.org/10.5194/acp-17-6895-2017, 2017.

Alfonso, L., Raga, G., and Baumgardner, D.: The validity of the kinetic collection equation revisited–Part 3: Sol–gel transition under turbulent conditions, Atmospheric Chemistry and Physics, 13, 521–529, 2013.

Alfonso, L., Raga, G. B., and Baumgardner, D.: The impact of fluctuations and correlations in droplet growth by collision–coalescence revisited–Part 2: Observational evidence of gel formation in warm clouds, Atmospheric Chemistry and Physics, 19, 14 917–14 932, 2019.

Ayala, O., Rosa, B., and Wang, L.-P.: Effects of turbulence on the geometric collision rate of sedimenting droplets. Part 2. Theory and parameterization, New Journal of Physics, 10, 075 016, https://doi.org/10.1088/1367-2630/10/9/099802, 2008.

Baker, M., Corbin, R., and Latham, J.: The influence of entrainment on the evolution of cloud droplet spectra: I. A model of inhomogeneous mixing, Quarterly Journal of the Royal Meteorological Society, 106, 581–598, https://doi.org/10.1002/qj.49710644914, 1980.

Beard, K. V.: Terminal velocity and shape of cloud and precipitation drops aloft, Journal of Atmospheric Sciences, 33, 851–864, 1976.

Blyth, A. M.: Entrainment in cumulus clouds, Journal of Applied Meteorology and Climatology, 32, 626–641, https://doi.org/10.1175/1520-0450(1993)032<0626:EICC>2.0.CO;2, 1993.

Bowen, E.: A new method of stimulating convective clouds to produce rain and hail, Quarterly Journal of the Royal Meteorological Society, 78, 37–45, 1952.

Chandrakar, K. K., Morrison, H., Grabowski, W. W., and Lawson, R. P.: Are turbulence effects on droplet collision–coalescence a key to understanding observed rain formation in clouds?, Proceedings of the National Academy of Sciences, 121, e2319664 121, 2024.

Chen, S., Xue, L., and Yau, M.-K.: Impact of aerosols and turbulence on cloud droplet growth: an in-cloud seeding case study using a parcel–DNS (direct numerical simulation) approach, Atmospheric Chemistry and Physics, 20, 10 111–10 124, https://doi.org/10.5194/acp-20-10111-2020, 2020.

Cooper, W. A., Lasher-Trapp, S. G., and Blyth, A. M.: The influence of entrainment and mixing on the initial formation of rain in a warm cumulus cloud, Journal of the Atmospheric Sciences, 70, 1727–1743, 2013.

Cotton, W. R.: Modification of precipitation from warm clouds—A review, Bulletin of the American Meteorological Society, 63, 146–160, 1982.

Devenish, B., Bartello, P., Brenguier, J., Collins, L., Grabowski, W. W., IJzermans, R., Malinowski, S. P., Reeks, M., Vassilicos, J., and Wang, L.: Droplet growth in warm turbulent clouds, Quarterly Journal of the Royal Meteorological Society, 138, 1401–1429, https://doi.org/10.1002/qj.1897, 2012.

Dziekan, P. and Pawlowska, H.: Stochastic coalescence in Lagrangian cloud microphysics, Atmospheric Chemistry and Physics, 17, 13 509–13 520, https://doi.org/10.5194/acp-17-13509-2017, 2017.

Dziekan, P., Jensen, J. B., Grabowski, W. W., and Pawlowska, H.: Impact of Giant Sea Salt Aerosol Particles on Precipitation in Marine Cumuli and Stratocumuli: Lagrangian Cloud Model Simulations, Journal of the Atmospheric Sciences, 78, 4127–4142, https://doi.org/10.1175/JAS-D-21-0041.1, 2021.

Exton, H., Latham, J., Park, P., Smith, M., and Allan, R.: The production and dispersal of maritime aerosol, in: Oceanic Whitecaps, pp. 175–193, Springer, 1986.

Feingold, G., Cotton, W. R., Kreidenweis, S. M., and Davis, J. T.: The impact of giant cloud condensation nuclei on drizzle formation in stratocumulus: Implications for cloud radiative properties, Journal of the atmospheric sciences, 56, 4100–4117, https://doi.org/10.1175/1520-0469(1999)056<4100:TIOGCC>2.0.CO;2, 1999.

Gillespie, D. T.: The stochastic coalescence model for cloud droplet growth, Journal of Atmospheric Sciences, 29, 1496–1510, https://doi.org/10.1175/1520-0469(1972)029<1496:TSCMFC>2.0.CO;2, 1972.

Grabowski, W. W. and Wang, L.-P.: Growth of cloud droplets in a turbulent environment, Annual review of fluid mechanics, 45, 293–324, https://doi.org/10.1146/annurev-fluid-011212-140750, 2013.

Hall, W. D.: A detailed microphysical model within a two-dimensional dynamic framework: Model description and preliminary results, Journal of Atmospheric Sciences, 37, 2486–2507, https://doi.org/10.1175/1520-0469(1980)037<2486:ADMMWA>2.0.CO;2, 1980.

Hoffmann, F. and Feingold, G.: Cloud Microphysical Implications for Marine Cloud Brightening: The Importance of the Seeded Particle Size Distribution, Journal of the Atmospheric Sciences, 78, 3247–3262, https://doi.org/10.1175/jas-d-21-0077.1, 2021.

Hoffmann, F. and Feingold, G.: A Note on Aerosol Processing by Droplet Collision-Coalescence, Geophysical Research Letters, 50, e2023GL103 716, 2023.

Hoffmann, F., Noh, Y., and Raasch, S.: The route to raindrop formation in a shallow cumulus cloud simulated by a Lagrangian cloud model, Journal of the Atmospheric Sciences, 74, 2125–2142, https://doi.org/10.1175/JAS-D-16-0220.1, 2017.

Hoffmann, F., Yamaguchi, T., and Feingold, G.: Inhomogeneous mixing in Lagrangian cloud models: Effects on the production of precipitation embryos, Journal of the Atmospheric Sciences, 76, 113–133, https://doi.org/10.1175/jas-d-18-0087.1, 2019.

Hudson, J. G. and Noble, S.: CCN spectral shape and cumulus cloud and drizzle microphysics, Journal of Geophysical Research: Atmospheres, 125, e2019JD031 141, 2020.

Jensen, J. B. and Nugent, A. D.: Condensational growth of drops formed on giant sea-salt aerosol particles, Journal of Atmospheric Sciences, 74, 679–697, https://doi.org/10.1175/jas-d-15-0370.1, 2017.

Johnson, D. B.: The role of giant and ultragiant aerosol particles in warm rain initiation, Journal of Atmospheric Sciences, 39, 448–460, https://doi.org/10.1175/1520-0469(1982)039<0448:TROGAU>2.0.CO;2, 1982.

Kostinski, A. B. and Shaw, R. A.: Fluctuations and luck in droplet growth by coalescence, Bulletin of the American Meteorological Society, 86, 235–244, https://doi.org/10.1175/BAMS-86-2-235, 2005.

Krueger, S. K., Su, C.-W., and McMurtry, P. A.: Modeling entrainment and finescale mixing in cumulus clouds, Journal of the atmospheric sciences, 54, 2697–2712, https://doi.org/10.1175/1520-0469(1997)054<2697:MEAFMI>2.0.CO;2, 1997.

Kuba, N. and Murakami, M.: Effect of hygroscopic seeding on warm rain clouds–numerical study using a hybrid cloud microphysical model, Atmospheric Chemistry and Physics, 10, 3335–3351, 2010.

Lasher-Trapp, S. G., Cooper, W. A., and Blyth, A. M.: Broadening of droplet size distributions from entrainment and mixing in a cumulus cloud, Quarterly Journal of the Royal Meteorological Society: A journal of the atmospheric sciences, applied meteorology and physical oceanography, 131, 195–220, 2005.

Latham, J., Bower, K., Choularton, T., Coe, H., Connolly, P., Cooper, G., Craft, T., Foster, J., Gadian, A., Galbraith, L., et al.: Marine cloud brightening, Philosophical Transactions of the Royal Society A: Mathematical, Physical and Engineering Sciences, 370, 4217–4262, 2012.

Li, X.-Y., Mehlig, B., Svensson, G., Brandenburg, A., and Haugen, N. E.: Collision fluctuations of lucky droplets with superdroplets, Journal of the Atmospheric Sciences, 2022.

Lim, J.-S. and Hoffmann, F.: Between Broadening and Narrowing: How Mixing Affects the Width of the Droplet Size Distribution, Journal of Geophysical Research: Atmospheres, 128, e2022JD037 900, 2023.

https://doi.org/10.5194/egusphere-2024-2636
Preprint. Discussion started: 29 August 2024

Low, T. B. and List, R.: Collision, coalescence and breakup of raindrops. Part I: Experimentally established coalescence efficiencies and fragment size distributions in breakup, Journal of Atmospheric Sciences, 39, 1591–1606, 1982.

Noh, Y., Oh, D., Hoffmann, F., and Raasch, S.: A cloud microphysics parameterization for shallow cumulus clouds based on Lagrangian cloud model simulations, Journal of the Atmospheric Sciences, 75, 4031–4047, https://doi.org/10.1175/JAS-D-18-0080.1, 2018.

O'Dowd, C. D., Smith, M. H., Consterdine, I. E., and Lowe, J. A.: Marine aerosol, sea-salt, and the marine sulphur cycle: A short review, Atmospheric Environment, 31, 73–80, https://doi.org/10.1016/S1352-2310(96)00106-9, 1997.

Onishi, R., Matsuda, K., and Takahashi, K.: Lagrangian tracking simulation of droplet growth in turbulence–turbulence enhancement of autoconversion rate, Journal of the Atmospheric Sciences, 72, 2591–2607, https://doi.org/10.1175/JAS-D-14-0292.1, 2015.

Pinsky, M., Khain, A., and Krugliak, H.: Collisions of cloud droplets in a turbulent flow. Part V: Application of detailed tables of turbulent collision rate enhancement to simulation of droplet spectra evolution, Journal of Atmospheric Sciences, 65, 357–374, https://doi.org/10.1175/2007jas2358.1, 2008.

Pruppacher, H. R. and Klett, J. D.: Microphysics of Clouds and Precipitation: Reprinted 1980, Springer Science & Business Media, 2012.

Saffman, P. and Turner, J.: On the collision of drops in turbulent clouds, Journal of Fluid Mechanics, 1, 16–30, 1956.

Seifert, A., Nuijens, L., and Stevens, B.: Turbulence effects on warm-rain autoconversion in precipitating shallow convection, Quarterly Journal of the Royal Meteorological Society, 136, 1753–1762, https://doi.org/10.1002/qj.684, 2010.

Shaw, R. A.: Particle-turbulence interactions in atmospheric clouds, Annual Review of Fluid Mechanics, 35, 183–227, 2003.

Shima, S.-i., Kusano, K., Kawano, A., Sugiyama, T., and Kawahara, S.: The super-droplet method for the numerical simulation of clouds and precipitation: A particle-based and probabilistic microphysics model coupled with a non-hydrostatic model, Quarterly Journal of the Royal Meteorological Society: A journal of the atmospheric sciences, applied meteorology and physical oceanography, 135, 1307–1320, https://doi.org/10.1002/qj.441, 2009.

Siebert, H., Lehmann, K., and Wendisch, M.: Observations of small-scale turbulence and energy dissipation rates in the cloudy boundary layer, Journal of the atmospheric sciences, 63, 1451–1466, https://doi.org/10.1175/JAS3687.1, 2006.

Squires, P.: The microstructure and colloidal stability of warm clouds: Part I—The relation between structure and stability, Tellus, 10, 256–261, 1958.

Sölch, I. and Kärcher, B.: A large-eddy model for cirrus clouds with explicit aerosol and ice microphysics and Lagrangian ice particle tracking, Quarterly Journal of the Royal Meteorological Society, 136, 2074–2093, https://doi.org/10.1002/qj.689, 2010.

Telford, J.: A new aspect of coalescence theory, Journal of Meteorology, 12, 436–444, https://doi.org/10.1175/1520-0469(1955)012<0436:ANAOCT>2.0.CO;2, 1955.

Teller, A. and Levin, Z.: The effects of aerosols on precipitation and dimensions of subtropical clouds: a sensitivity study using a numerical cloud model, Atmospheric Chemistry and Physics, 6, 67–80, 2006.

Unterstrasser, S., Hoffmann, F., and Lerch, M.: Collisional growth in a particle-based cloud microphysical model: insights from column model simulations using LCM1D (v1. 0), Geoscientific Model Development, 13, 5119–5145, https://doi.org/10.5194/gmd-13-5119-2020, 2020.

Wang, L. and Grabowski, W. W.: The role of air turbulence in warm rain initiation, Atmospheric Science Letters, 10, 1–8, https://doi.org/10.1002/asl.210, 2009.

Wang, L., Xue, Y., Ayala, O., and Grabowski, W. W.: Effects of stochastic coalescence and air turbulence on the size distribution of cloud droplets, Atmospheric research, 82, 416–432, https://doi.org/10.1016/j.atmosres.2005.12.011, 2006.

https://doi.org/10.5194/egusphere-2024-2636
Preprint. Discussion started: 29 August 2024

Wilkinson, M.: Large deviation analysis of rapid onset of rain showers, Physical review letters, 116, 018 501, https://doi.org/10.1103/PhysRevLett.116.018501, 2016.

Woodcock, A. H.: Salt nuclei in marine air as a function of altitude and wind force, Journal of Atmospheric Sciences, 10, 362–371, https://doi.org/10.1175/1520-0469(1953)010<0366:SNIMAA>2.0.CO;2, 1953.

Yin, Y., Levin, Z., Reisin, T. G., and Tzivion, S.: The effects of giant cloud condensation nuclei on the development of precipitation in convective clouds—A numerical study, Atmospheric research, 53, 91–116, https://doi.org/10.1016/S0169-8095(99)00046-0, 2000.